Jour. Geol. Soc. India (2022) 98:795-804
https://doi.org/10.1007/s12594-022-2070-6

ORIGINAL ARTICLE

Assessment of Seismic Vulnerability using the Ambient Noise Recordings in Cachar Fold Belt, Assam

Kuldeep[1,*], Bharath Shekar[1], Gollapally Mohan[1] and Sunil Kumar Singh[2]

[1]Department of Earth Sciences, Indian Institute of Technology Bombay, Mumbai - 400 076, India
[2]Oil and Natural Gas Corporation, Jorhat - 785 704, India
E-mail: kuldeepgeos@iitb.ac.in

Received: 13 October 2021/ Revised form Accepted: 31 January 2022

ABSTRACT

Northeast India is a seismically active region, with frequent major earthquakes. The impact of seismicity can be assessed by using the values fundamental resonant frequency (F_0) and the site amplification factor (A_0) to derive the seismic vulnerability index (K_g). In 2011, a network of 65 stations was installed in the Cachar fold belt, Assam to continuously record data for a continuous period of eleven months. In this study, the horizontal-to-vertical spectral ratio (H/V) method is employed to identify the resonant frequencies and site amplification factors using ambient noise data to assess the seismic hazard potential in the Cachar fold belt. The amplification factors ranged between 1.15 to 6, while the resonance frequencies varied between 0.25 to 5 Hz. The ambient noise interferometry is utilized to estimate surface waves between station pairs and invert the group velocity dispersion curves for the near-surface S-wave velocities. The S-wave velocity for the basement rocks varied between 600 to 1600 m/s. The S-wave velocities are in turn used to derive an empirical relationship between resonant frequency and alluvium thickness valid for the study region. It is found that stations located at regions with subsurface anticlines had a relatively high resonance frequency and low amplification factor, whereas receivers in synclinal locations and with a thick layer of alluvium sedimentary deposits have a substantially higher site amplification factor and lower resonant frequencies. Further, it is observed that regions with a substantial alluvium sediment cover and near the course of the Barak river are more seismically vulnerable and susceptible to natural hazards.

INTRODUCTION

The use of ambient noise data for determining the shallow structure of basement rocks has gained popularity in recent decades. In microzonation studies or site evaluation for key infrastructure, evaluating site-effects owing to local geology or topography has become a necessity. The horizontal-to-vertical spectral ratio (H/V or HVSR) technique has found widespread use in evaluation of local site characterization (Nakamura, 1989; Lermo et al, 1993; Bard, 1999; Acerra et al, 2004, Bonnefoy-Claudet et al, 2009, Surve et al, 2010, Sivaram et al, 2012, Molnar et al, 2018, Nagamani et al, 2020), seismic microzonation (Mukhopadhyay et al, 2004, Nath et al, 2008) and groundwater studies (Rigo et al, 2020). Nogoshi and Igarashi (1971) initially proposed the HVSR method, but it was popularised by Nakamura (1989) and it became to be known as the "Nakamura technique". The Nakamura technique has been thoroughly described in Nakamura (2000) and Ibs-von Seht and Wohlenberg (1999).

Lachet and Bard (1994) conducted a study utilizing six basic subsurface formations and a combination of contrast variations in wave velocity and ground layer thickness, demonstrating the relationship between the dominant frequency and geological conditions. Fah (2004) investigated the fluctuation of the resonance frequency, along with the amplitude and polarization of seismic data as a function of the structure and source positions. Sylvette et al, (2005) demonstrated the impact of source spatial position on the H/V shape and concluded that H/V peaks are due to S-wave resonance of the head waves when ambient noise sources are in the bedrock. A single peak is observed for the H/V curves if the sources are inside the sedimentary layer and close to the receiver, while two peaks are observed if the sources are far from the receivers. The Nakamura method has been outlined in detail by Nakamura (2019) and suggestions are given to avoid potential pitfalls in the interpretation. In this study, Nakamura's technique is applied to assess the seismic vulnerability of the ground and structures using the fragility index, or more popularly known as the seismic vulnerability index (K_g). The empirical relationship between the predominant frequencies and the sediment thickness in the region is estimated by utilising information derived from ambient noise interferometry.

Ambient noise recorded as part of passive seismic data can be processed by interferometry to obtain the empirical Green's function (Rickett & Claerbout, 1999; Lobkis & Weaver, 2001; Wapenaar, 2004). Sources of ambient noise may either be of natural (e.g. ocean microseisms) or cultural (e.g. traffic noise, induced seismicity) in origin. Green's functions retrieved from ambient noise interferometry ideally contain the complete response of the medium between the virtual source and receiver (Waapenaar, 2004). Seismic interferometry applied to ambient noise data can yield surface waves (Shapiro and Campillo, 2004; Bensen et al, 2007; Yang & Ritzwoller, 2008) or reflected body waves (Draganov et al, 2009; Nakata et al, 2015). Cultural noise typically has frequency content above 1 Hz (Peterson, 1993) and has been used to obtain shallow subsurface information with cross-correlation interferometry. For example, Chavez & Luzon (2005) retrieved Rayleigh and Love waves in the frequency range of 3.6 – 6 Hz and 6 – 20 Hz, respectively. Traffic noise from highways was utilised by Behm et al, (2014) to obtain Rayleigh and Love waves in the 2 – 6 Hz bandwidth. Here, cultural noise is utilized to obtain surface waves between pairs of stations. The dispersion curves of the obtained surface

waves are inverted for shallow S-wave velocities useful to obtain the relationship between resonance frequencies and sediment depth.

The organisation of the article is as follows: first, an introduction of the geology and seismicity of the study area, followed by a description of the instrumentation and data acquisition. In the methodology section, the application of ambient noise interferometry is outlined to retrieve surface waves and their inversion for shallow S-wave velocity profiles. Then the application of the HVSR method is discussed to obtain resonant frequency and site vulnerability index. Finally, interpretation of the obtained results to assess the seismic vulnerability of the study area.

GEOLOGICAL SETTING AND SEISMICITY

Northeast India is one of the world's most seismically active regions, and a seismicity map for the region is displayed in Fig.1. As per the Bureau of Indian Standards, the study regions come under the seismic Zone-V (Very Severe Intensity Zone). Walling et al, (2009) have given a detailed overview of a broad study on microzonation studies in India. There have been many large earthquakes in the region like the 1897 Great earthquake (Ms 8.7), the Cachar earthquake (1869, Mw 7.4), the Assam earthquake (1950, Mw 8.5), and about 20 large earthquakes (M > 7.0) since 1869 (Kayal et al, 2012). Another earthquake in Cachar on December 30, 1984, despite being of comparably low magnitude (M 5.8), resulted in the loss of life and caused severe damage to property (GSI, 2000).

The Cachar area is part of the Assam-Arakan geo-synclinal Basin's N-S compressional thrust and fold belt with a spread of around 7000 square kilometers and is a potential hydrocarbon-bearing zone (Saha et al, 2008). The Cachar region is defined topographically by a central E-W trending transverse low that defines the valley's course of the Barak river. The drainage in the region is provided by the Barak river, which is clearly influenced by the area's geographical structure. The Cachar fold belt is distinguished by the presence of broad synclines and tight anticlines in the Tripura-Cachar region, which includes a number of hydrocarbons-producing fields. The majority of these fields in Assam's Cachar region occur at the culmination of anticlinal structures (Mazumder et al, 2016). The Assam-Arakan fold-belt formed as an accretionary wedge on the subducting Indian crust beneath the Burma plate (Dasgupta & Nandy, 1995). The Cachar region has a thick column of clastic deposits ranging in age from Paleocene to Recent, consisting of sandstone, siltstone, shale, and claystone. Figure 2 shows the surface geological map of the Cachar region. The main lithostratigraphic units in the Cachar region are Dihing (Pleistocene-Holocene), Dupitila (Pliocene- Pleistocene), Tipam (Miocene-Pliocene), Surma (Miocene), Barail (late Eocene- Oligocene), and Disang (Paleocene- Eocene) (see Chatterjee et al, 2018; Garain et al, 2019).

INSTRUMENTATION AND DATA

The Oil and Natural Gas Corporation (ONGC) Ltd. installed a network of 65 wideband seismic stations in the Cachar region of Assam, India, to assess local and regional seismicity and to image subsurface structures. The stations consisted of Seismotech - S100, a wide-band three-component velocity output seismic sensor, and a bandwidth of 0.1-100 Hz with a flat response from 1-40Hz. The design of the sensor is based on the force-balance principle, using three simple geophone elements. The seismometers were equipped with S-24 digital recorders with 24-bit resolution. The seismometers were placed in cement-cased boreholes at depths ranging from 6 to 8m. The seismometers continuously recorded the data over a period of eleven months from January to November 2011. The location of the stations is shown in Fig.3.

METHODOLOGY

In this study, the horizontal to vertical spectral ratio (HVSR) method is used to obtain the resonant frequencies and site amplification factor for receiver locations. Then the resonant frequencies and site amplification factors is used to estimate the seismic vulnerability index (K_g) in the region. The ambient noise interferometry is applied to estimate surface waves between receiver pairs and invert the surface

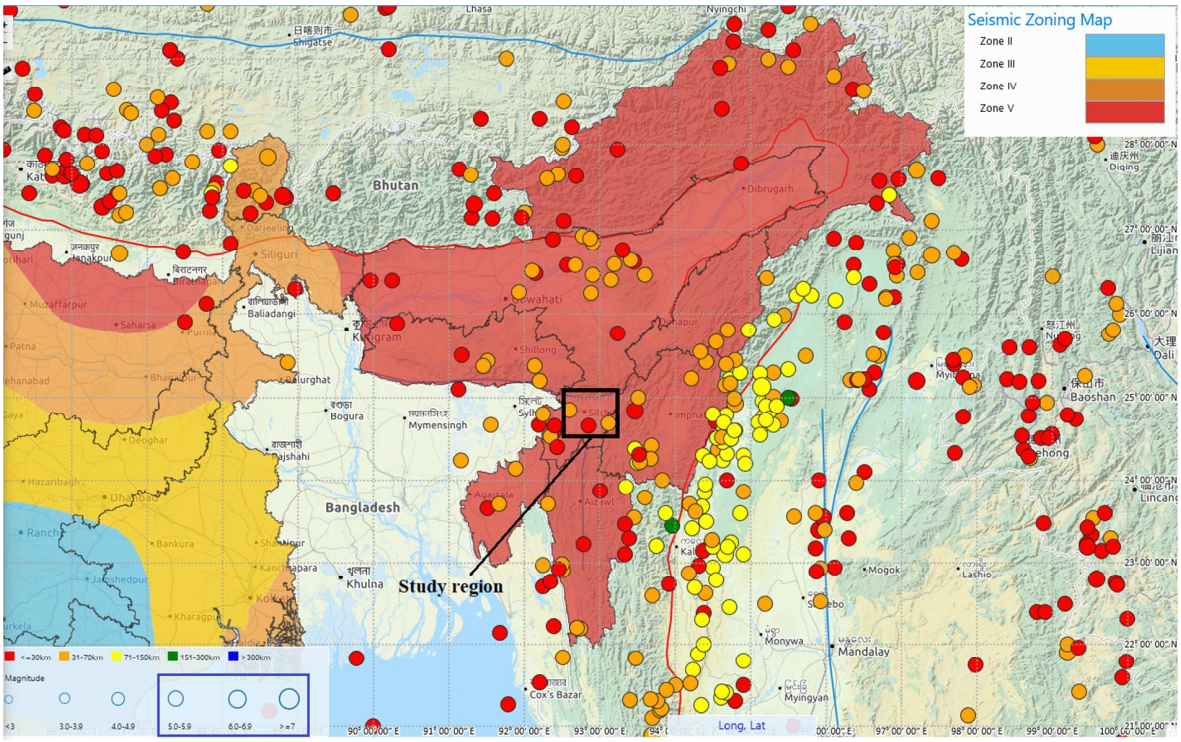

Fig.1. Distribution of large magnitude earthquakes (>5) in and around the study region in Northeast India over the last 50 years (source: National Center for Seismology - https://seismo.gov.in/MIS/riseq/Earthquake/archive)

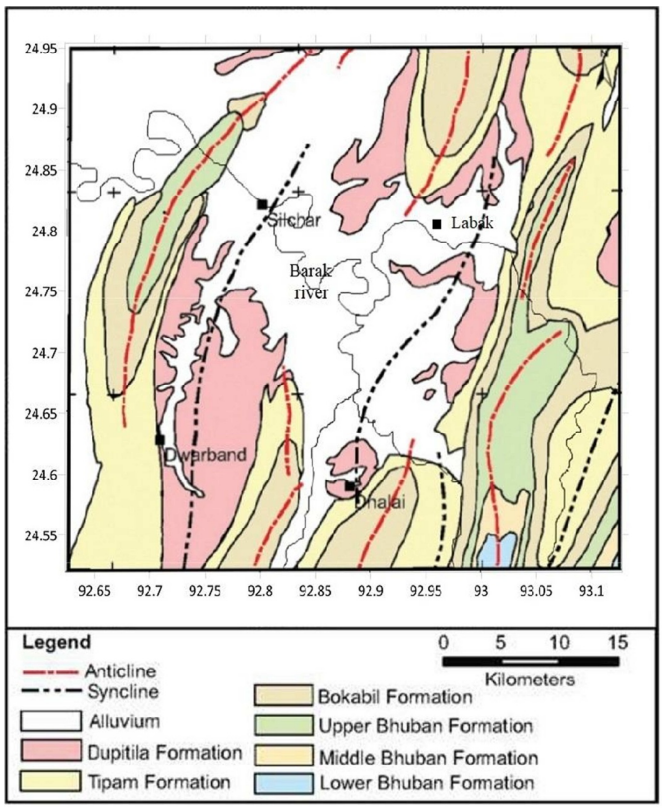

Fig. 2. Surface geological map of the Cachar region, modified after Garain et al (2019).

wave dispersion curves to obtain the S-wave velocity profiles in the region. The obtained S-wave velocities for the base rocks are utilized to develop an empirical relationship between resonant frequency and sediment thickness that is valid for the study region. The methods employed in the study are described in detail in the following subsections.

Horizontal to Vertical Spectral Ratio (HVSR)

Site response studies are used to assess the fundamental natural frequency or resonance frequency of site amplification for a given site, which is a key parameter in determining the seismic hazard potential for a certain area. The HVSR of ambient noise is a simple, fast, and non-intrusive approach for determining the fundamental natural frequency and amplification characteristics of the surface layer from the measurement only at the ground surface. The process involves calculating the horizontal and vertical components' Fourier spectra and calculating their ratio (H/V) and the peak of the H/V curve corresponding to the fundamental natural frequency of the soil deposits (Surve and Mohan, 2010). The HVSR value is connected to the soil's solidity and amplification factor and can be used to assess the soil's properties (Nakamura, 2000). It is related to the geotechnical conditions, soil type, and sediment layer thickness.

Resonance Frequency and Site Amplification Factor Measurements

The H/V is computed using the spectrum ratio between two horizontal components and one vertical component, using following expression:

$$(H/V) = \sqrt{(NS^2 + EW^2)/2VT^2} \quad (1)$$

where H represents the horizontal component spectrum and V represents the vertical component spectrum. NS and EW are the two horizontal components of the recorded signal in the directions of north-south component and east–west, respectively. VT represents the vertical component of the recorded signal. At a given site, the resonance frequency (F_0) or dominant frequency is the frequency at which the H/V reaches its maximum, and the amplification factor (A_0) is the magnitude of this frequency. For HVSR processing, an open-source Python library "hvsrpy" is used (Vantassel, 2020).

The SESAME (2004) recommendations are followed for reliable HVSR estimates. To identify even the extremely low frequencies, window length of 60 seconds and a record period of 2 hours is utilized, which is almost four times the minimum suggested signal

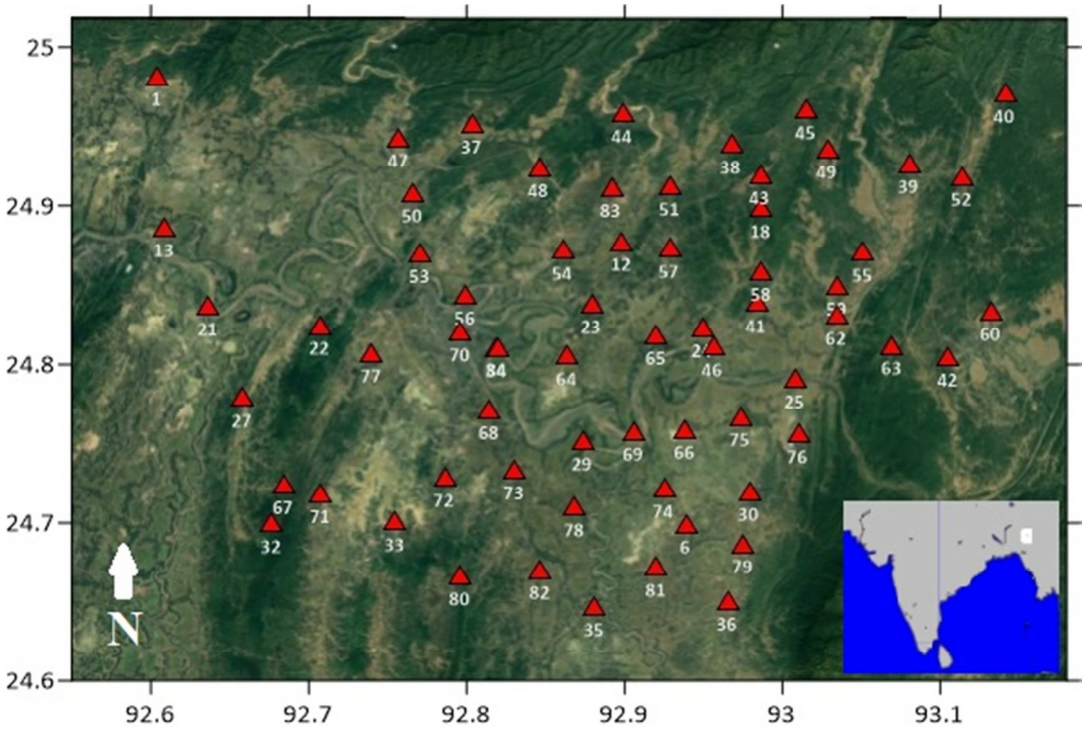

Fig. 3. A satellite map of the region with the geographical distribution of stations (red triangles).

record time duration for the selected window length. To prevent any cultural noise, the data recorded late at night, between 1 a.m. and 3 a.m were used. An automated frequency-domain window-rejection technique was employed in hvsrpy to reject spurious temporal frames, which improves the clarity and sharpness of the median HVSR curve (Cox et al. 2020). If the HVSR curve has a distinct peak (or peaks), the lowest frequency peak gives an estimate of fundamental natural frequency. The HVSR curves with no identifiable peak at 10 stations is received, which did not satisfy SESAME reliability and clarity guidelines, and these stations were eliminated from further investigation. Figurs 4 show the H/V measurements at receiver stations 64. In the HVSR measurements, we get a maximum amplification factor of around 6 and a range of resonance frequency up to 5 Hz.

Figure 5 displays the obtained results of fundamental natural frequency variations on the map. The values larger than four is rounded off to a value of four just for plotting purposes, to improve visual clarity. Natural neighbor interpolation is used to create the contours in the backdrop in Fig.5. Figure 6 shows the distribution of site amplification for the corresponding resonance frequencies in Fig. 5. A high site amplification with low resonance frequencies in syncline regions of the Silchar and Labak area having a thick sediment cover is observed, while the surrounding mountainous regions with anticline formations showed high resonance frequencies with lower amplification factors.

Sediment Layer Thickness and Shear-wave Velocity

The resonance frequency and velocity of the shear-wave (S-wave) are related to the thickness of the sediment. The link between these values may be explained by a simple model consisting of two layers of substrate, with hard rock in the basement with S-wave velocity V_{sb} being covered by a layer of soft sediments of thickness Z and S-wave velocity V_s. The resonance frequency is reached for the site when the thickness of the sediment is an odd multiple of a quarter of the wavelength, and the transfer function reaches its maximum value at the resonant frequencies (F_r) (Ibs-von Seht & Wohlenberg, 1999):

$$F_r = (nV_s) / (4z), \quad (n = 1, 3, 5,...) \tag{2}$$

For the fundamental natural frequency, n = 1, the expression has the following form:

$$F_0 = (V_s) / (4z), \tag{3}$$

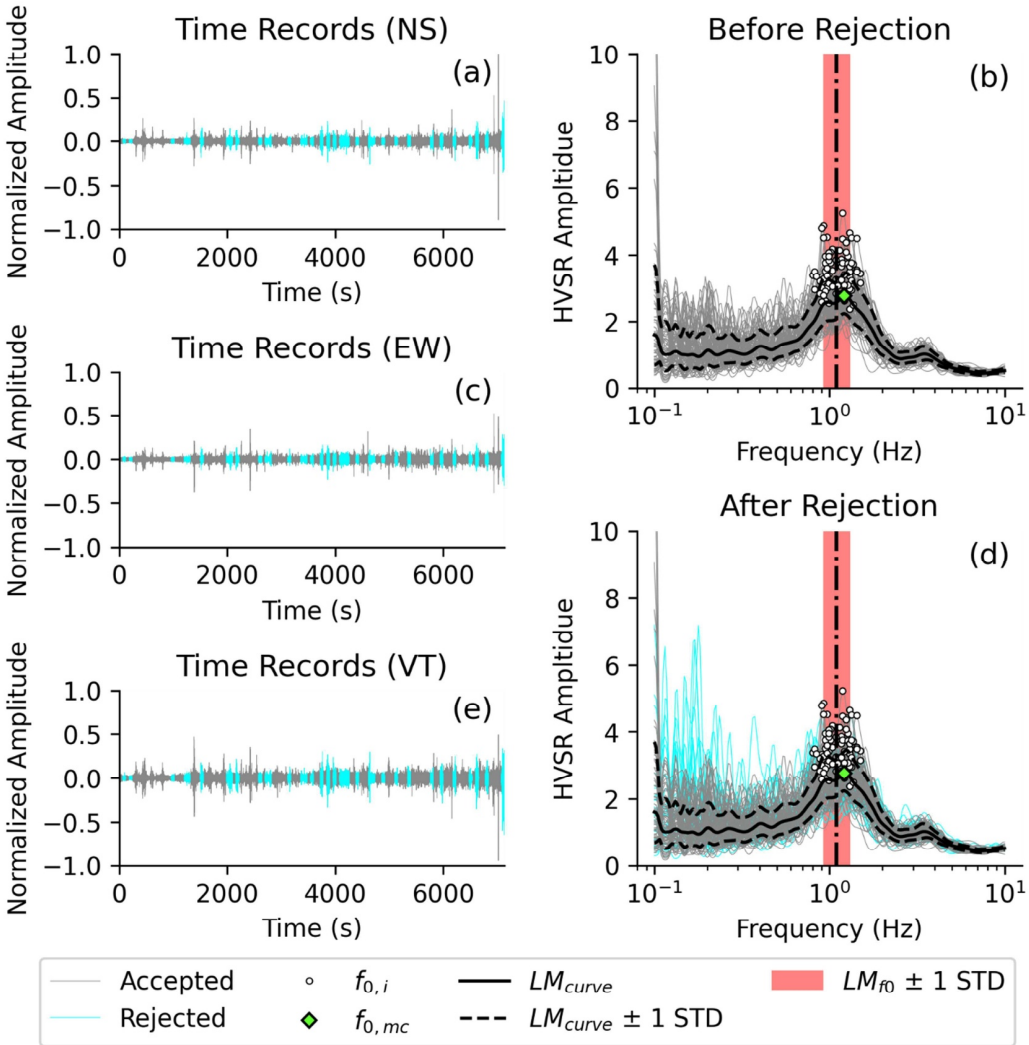

Fig.4. HVSR measurement from the receiver station 64. Ambient noise recordings of the three orthogonal components **(a)** NS for North-South component, **(b)** EW for East-West component, and **(c)** VT for Vertical component. HVSR curve (gray lines) plots **(d)** for all the time windows, and **(e)** after rejection by the FWA algorithm (shown in cyan). The solid black line represents the log-normal median curve, while the dashed black lines indicate the HVSR curve's 68 percent confidence interval. The apex of the median curve is shown by the green diamond, and its values in (e) yield F_0 and A_0 estimations.

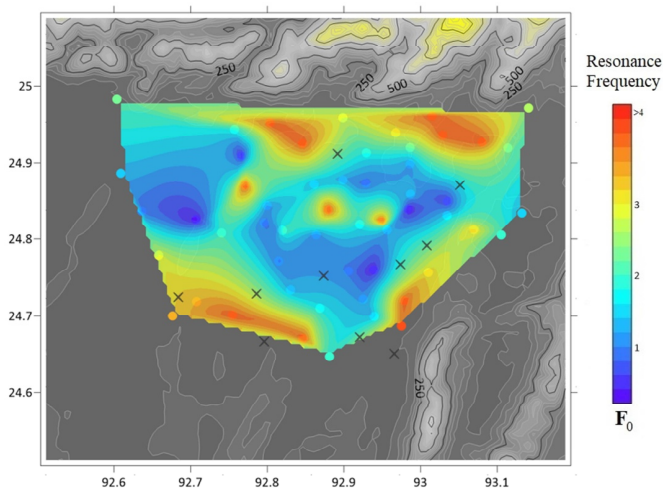

Fig. 5. A map depicting variation of resonance frequency (F_0) in the study region. Crosses indicate sites where the HVSR findings did not satisfy the reliability and stability criteria. To facilitate visual clarity, values larger than four are rounded down to four. The contours in the background are obtained from natural neighbor interpolation.

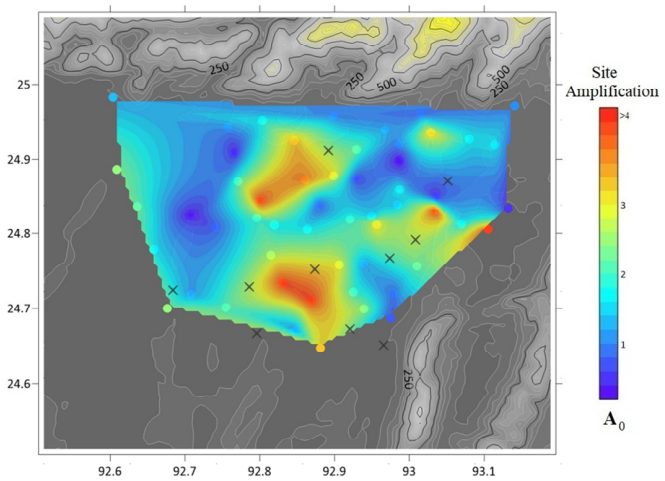

Fig. 6. A map depicting variation of site amplification factor in the study region. Crosses indicate sites where the HVSR findings did not satisfy the reliability and stability criteria. To facilitate visual clarity, values larger than four are rounded down to four. The contours in the background are obtained from natural neighbor interpolation.

If the resonant frequency (F_0) is known and site amplification (A_0), as well as the S-wave velocity of the base rock (V_{sb}) in a given area, we may estimate V_s and Z of the respective location using the following relations (Nakamura, 2019):

$$V_s = (V_{sb}) / A \,, \tag{4}$$

$$Z = (V_{sb}) / (4AF_0). \tag{5}$$

Using HVSR studies, we have obtained the resonant frequency and corresponding site amplification at the receiver locations. Seismic interferometry technique that yields surface waves by the cross-correlation of ambient noise recording data from a pair of receiver stations (e.g., Shapiro et al, 2005; Bensen et al, 2007). The dispersion curves of the retrieved surface waves are then inverted to obtain the S-wave velocity of the base-rock (V_{sb}) in the study area.

Ambient Noise Interfermetry

The vertical component data from wide-band stations is utilized to perform cross-correlation interferometry and obtain Rayleigh waves. The processing methodology is similar to that outlined in Bensen et al., (2007) with suitable modifications for the data from the study area. Then the Rayleigh wave group velocity dispersion curves was inverted by the perturbational inversion algorithm of Haney and Tsai (2017) to derive the S-wave velocity depth profiles. The methodology adopted is outlined in the following subsections in detail.

Data-preprocessing

To gain insight into the character of the ambient noise data, the probabilistic power spectral density (PPSD) defined in McNamara and Buland (2004) was computed and implemented by the "Obspy" package (Krischer et al., 2015) with one-minute data segments and overlap of ten seconds over the entire period of recording. Figure 7 shows the PPSD computed using the entirety of data collected at a representative location (station 64), along with Peterson's new low noise model (NLNM) and new high noise model (NHNM) (Peterson, 1993). The PPSD plot indicates that low-frequency ambient noise between 0.1 to 1 Hz has a greater probability of occurrence, although the energy is lower than the NLNM.

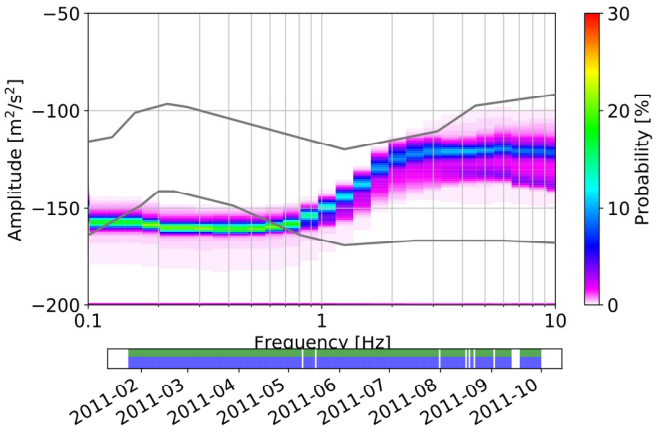

Fig.7. The probabilistic power spectral density function computed using the entirety of the data recorded at station 64.

The low-frequency ambient noise could have its source of origin in the secondary microseism, although a significant peak is not seen in the secondary microseism band at around 0.2 - 0.4 Hz. The data however do exhibit significant energy between 1 to 10 Hz expected for noise sources with an anthropogenic origin (traffic and cultural noise), although the probability of occurrence is lower than that of lower frequency data. The difference in probabilities can be explained by the fact that while low-frequency ambient noise due to the ocean-induced secondary microseism is persistent, anthropogenic sources of noise are sporadic.

Waveforms from earthquakes contain significant amplitudes, which can cause cross-correlograms to be biased. By muting the recorded seismograms around the respective arrival periods, signals matching to catalogued earthquakes can be avoided. Temporal normalization techniques like sliding window mean-normalization, automatic gain control (AGC) or one-bit normalization can mitigate the bias introduced by large magnitude signals (Bensen et al, 2007). Here, we apply one-bit normalization to the vertical component data, which entails keeping simply the sign of each sample in the records (+1 or 1). One-bit correlation effectively removes the bias due to large amplitude signals and can yield correlograms with an enhanced signal-to-noise ratio (Hanasoge et al., 2013). Post the One-bit normalization of data, we apply spectral whitening to reduce spectral imbalance from potential agricultural and industrial sources in the densely populated Cachar region (Census of India, 2011).

Cross-correlation and Frequency Time Analysis

It is common practice to use day-long time windows for cross-correlation in global studies (e.g. Bensen et al., 2007; Yang et al., 2008). However, the crosscorrelation window in local studies ranges from a few minutes (Mordret et al., 2013; Behm et al., 2014) to hours (de Ridder and Biondi, 2015; Zigone et al., 2015; Obermann et al., 2016). A ten-minute window was used to compute the cross-correlations as it allows for sufficient time for the surface waves to traverse the length of the array. Then the correlograms were stacked over the period of recording and observe a gradual emergence of surface waves.

Figure 8 shows one such empirical cross-correlogram stack corresponding to the receiver pair 23-64, with receiver 23 as the virtual source. The causal part of the correlogram is more dominant due to the fact that the virtual source (receiver 23) was located nearer than receiver 64. Further, the stacked correlograms were dominated by energy in the 1-3 Hz band. The dispersion curves were measured using frequency-time analysis (Dziewonski et al., 1969; Bensen et al., 2007). Frequency-time analysis or FTAN involves the application of Hilbert transform to convert the correlogram stacks into analytical signals. The envelope and phase functions derived from the analytical signals are then filtered by narrow-band Gaussian filters. The peak of the envelope function represents the arrival time of the wave packet as a function of the frequency, and this is used to calculate the group velocity dispersion curves for the surface waves. The FTAN diagram for the cross-correlation stack from Figure 8 is shown in Figure 9. The Rayleigh wave group velocity dispersion curves obtained by picking the ridge of the FTAN images are plotted in Figure 10, with the error bars corresponding to the margin of velocity where the FTAN value reduces to 70% of the peak value. It is assumed that the error bars correspond to one standard deviation.

Inversion of dispersion curves

The Rayleigh wave group velocity dispersion curves were inverted by the perturbational inversion algorithm of Haney and Tsai (2017). The initial model for the inversion is obtained using the Dix-like inversion method of Haney and Tsai (2015). The Dix-like inversion

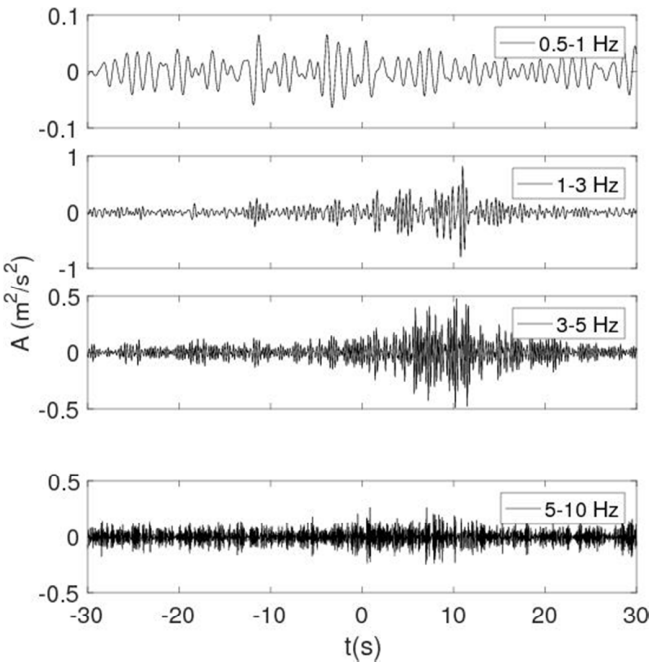

Fig. 8. Cross-correlogram stack obtained for the receiver pair 23 – 64 as a function of several frequency bands. Station 23 corresponds to the virtual source.

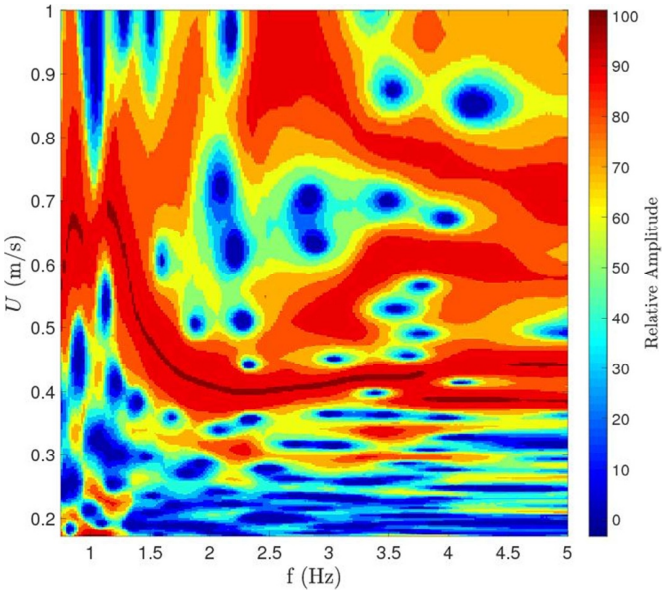

Fig. 9. FTAN analysis for the cross-correlogram stack from Fig.8.

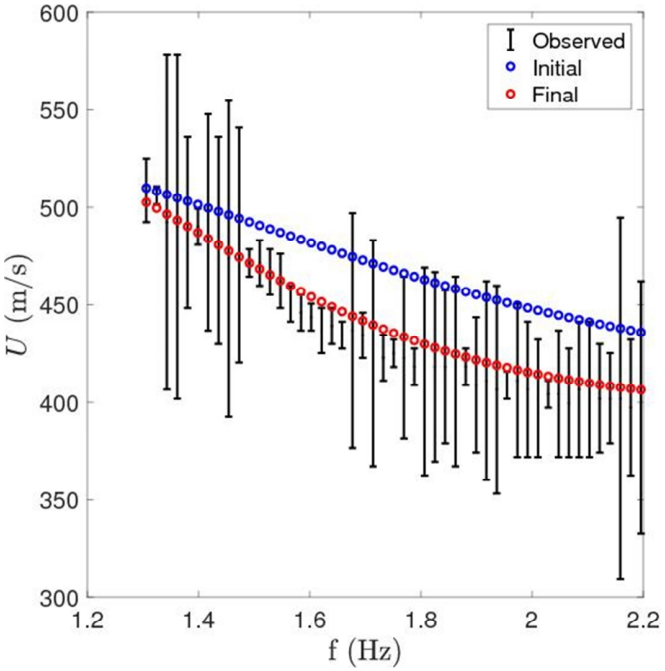

Fig. 10. Group velocity dispersion curve along with error bars (black) obtained from the FTAN image in Figure 9. The dispersion curve fit by the initial model obtained from Dix-like inversion is shown in blue and that from perturbational inversion is shown in red.

applied here builds the initial model as a function of depth by assuming that the Rayleigh wave at a given frequency propagates in a homogeneous medium. Then, the initial S-wave velocity is obtained from the group velocity, and the P-wave velocity is calculated from a user-supplied value of Poisson's ratio. For the clayey sediments expected in the study area, we utilized a Poisson's ratio of 0.40, which is an average estimate. A uniform density of 2000 k_g/m^3 is assumed. Following the initial model building from Dix-like inversion, the final S-wave velocity profiles are obtained using the perturbational inversion algorithm of Haney and Tsai (2017). The final model obtained from perturbational inversion fits the dispersion data more closely than the initial model obtained from the Dix-like inversion (Fig.10). Figure 11 displays the initial and final S-wave velocities obtained from Dix-like

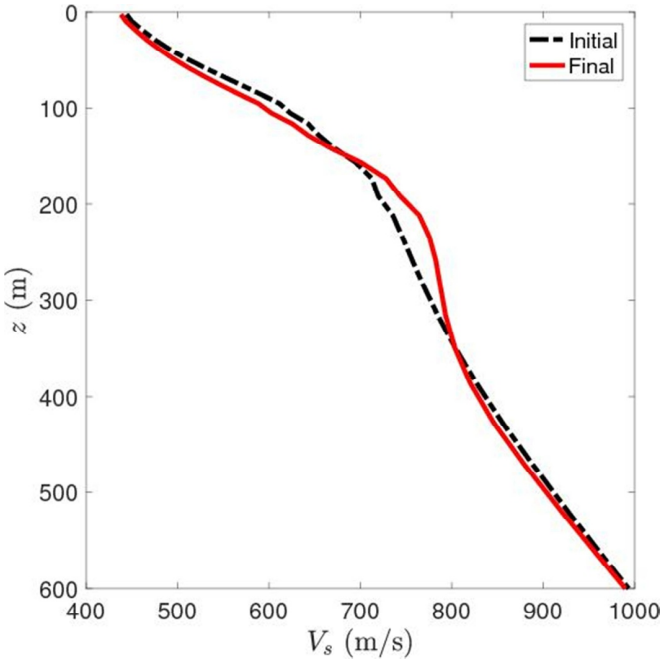

Fig. 11. S-wave velocity profiles corresponding to the initial model obtained from Dix inversion (black) and final model obtained from perturbational inversion (red) for the dispersion curve corresponding to the receiver pair 23 – 64.

and perturbational inversion, respectively, as functions of depth corresponding to the receiver pair 23-64.

Figure 12 shows inverted S-wave velocity profiles acquired in a similar manner from various other receiver pairs. We found that variations of V_{sb} in the study region are in the range of 600 to 1600 m/s after examining the obtained S-wave velocity depth profiles. The V_{sb} estimates, as well as HVSR results, are used in Equations 4 and 5. Table 1 lists all of the estimated parameters obtained at various receiver stations.

RESULTS

From the S-wave depth profiles acquired by ambient noise interferometry, we determined the base-rock shear-wave velocity (V_{sb}) between receiver pairs. While ambient noise interferometry helps to reduce acquisition costs, pairwise comparisons across all sensors make it a time-consuming and computationally expensive operation to perform over a dense network (Martin, 2020). On the other hand, the HVSR method is a very quick and low-cost single-site subsurface investigation technique. An attempted is made to blend the two approaches and gain the benefits of both. Using ambient noise interferometry, it is possible to identify the S-wave velocity profiles across a pair of receiver stations, from which one get an approximate estimate of S-wave velocity in base-rock near a station. The fundamental natural frequency (F_0) is used and site amplification (A_0) estimates obtained from the HVSR technique, along with an estimate of the S-wave velocity of the base-rock (V_{sb}) from ambient noise interferometry near the corresponding station to determine the Vs and Z at the sites corresponding to the respective receivers (Table 1). Ibs-von Seht and Wohlenberg (1999) derived a relation between sediment cover thickness and H/V spectrum peak frequency, a method that many researchers have since adopted (e.g. Delgado, 2001; Parolai et al., 2002; Mundepi et al, 2009; Dinesh et al, 2010). According to Ibs-von Seht and Wohlenberg (1999), the relationship between F_0 and Z has the following expression:

$$Z = aF_0^b \tag{6}$$

where a and b are constants. When b is negative, the resonant frequency falls as the thickness of the strata increases. Using the data from Table 1, we performed a regression analysis to obtain the best approximation for constants a and b that are valid in the study region. The relationship obtained from the regression analysis reads:

$$Z = 117.6F_0^{-0.896} \tag{7}$$

Figure 13 showcases the regression fit for Equation 7. A similar trend was found in empirical constants as in previous worldwide studies, with slight variances accounting for differences in soil characteristics in our study region. According to Equations 3 and 5, sites with high resonance frequencies should be related to thin sediment layers, whereas sites with low resonance frequencies should be related to thick sediment layers.

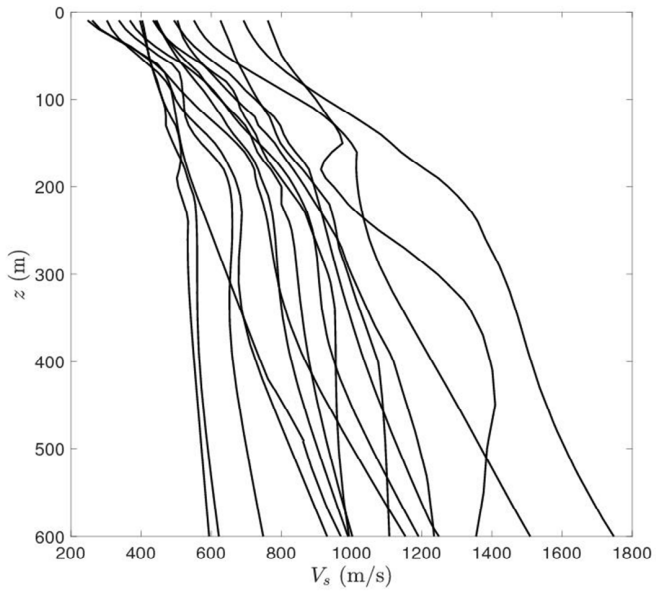

Fig. 12. S-wave velocity profiles obtained from ambient noise interferometry for the various receiver pairs in the study region.

Table 1. Measurement and calculated parameters of stations used in the estimation of empirical constants for Equation 6 shown in Figure 13. Base-rock S-wave Velocity estimates are from the S-wave depth profiles obtained using ambient-noise interferometry.

Sr. No.	Stat. No,	V_{sb} (m/s)	V_s (m/s)	H (m)	F_0 (Hz)	A_0 Value	Kg Value	Kg Class	Soil Class
1	6	700	250	44.6	1.4	2.8	5.6	III	D
2	12	950	296.9	61.8	1.2	3.2	8.5	III	D
3	18	1000	862.1	189.1	1.14	1.16	1.6	I	B
4	23	800	526.3	29.2	4.51	1.52	0.5	I	B
5	34	800	358.7	71.7	1.25	2.23	3.9	II	D
6	41	900	463.9	463.9	0.25	1.94	15.1	IV	C
7	42	1000	256.4	35.6	1.8	3.9	8.6	III	D
8	43	1200	681.8	77.5	2.2	1.76	1.4	I	C
9	46	1000	303	63.1	1.2	3.3	9.2	III	D
10	57	950	669	199.1	0.84	1.42	2.4	I	C
11	58	900	391.3	69.9	1.4	2.3	3.8	II	C
12	60	1000	769.2	143.5	1.34	1.3	1.2	I	B
13	64	800	346.3	82.5	1.05	2.31	5.1	III	D
14	66	1200	648.6	491.4	0.33	1.85	10.3	IV	C
15	68	800	280.7	73.9	0.95	2.85	8.6	III	D
16	71	1500	815.2	59.8	3.41	1.84	1.0	I	B
17	74	1200	500	113.6	1.1	2.4	5.4	III	C
18	77	1200	769.2	96.2	2	1.56	1.2	I	B
19	79	1100	748.3	49.5	3.78	1.47	0.6	IV	C
20	84	1200	545.5	64.9	2.1	2.2	2.5	III	C

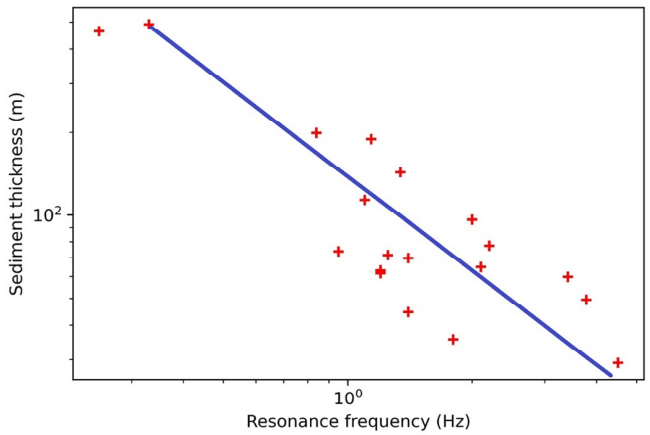

Fig. 13. The empirical constants in Equation 6 were obtained via regression analysis by using inputs from Table 1.

The V_s values were estimated for stations that were not included in ambient noise interferometry but had reliable HVSR measurements using Equations 7 and 3. Figure 14 shows the distribution of obtained V_s values of the sedimentary layer in the study region. The S-wave velocities vary greatly due to the lateral heterogeneities in the sedimentary basin. The soil in the study region is predominantly interpreted as belonging to NEHRP classes D, C, and B according to the NEHRP (1997) soil classification standards for the top sedimentary layer.

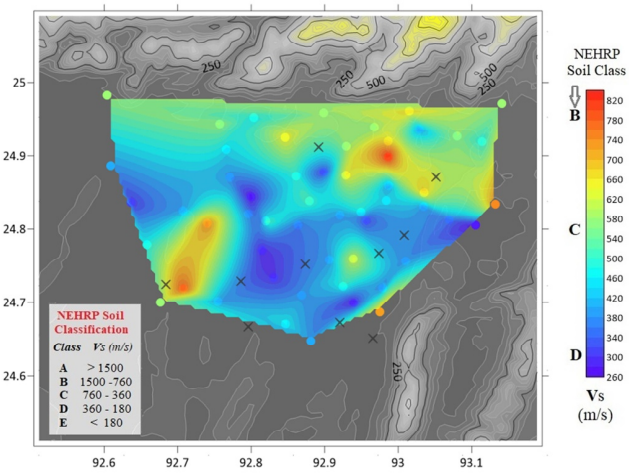

Fig. 14. The distribution of average S-wave velocity (Vs) for the study area calculated using Equations 4 and 6. Crosses indicate sites where the HVSR findings did not satisfy the reliability and stability criteria. The contours in the background are obtained from natural neighbor interpolation.

Determination of Seismic Vulnerability Index (Kg)

Seismic waves exert stress on the buildings and ground during propagation. The structure may collapse if the resulting strain exceeds the strain limit. The occurrence of earthquake damage is well recognized to be dependent on the strength, period, and duration of seismic events, and these parameters are influenced by seismic response characteristics of surface ground and structures (Nakamura, 2000). To assess the potential damage caused by earthquakes, Nakamura (1997) introduced a ground fragility index, commonly known as the Seismic vulnerability index (K_g). It can assess the risk of soil liquefaction and earthquake damage using the relevant information from the HVSR of ambient noise, giving us vital information about the seismic hazard potential in a specific region. Nakamura proposed

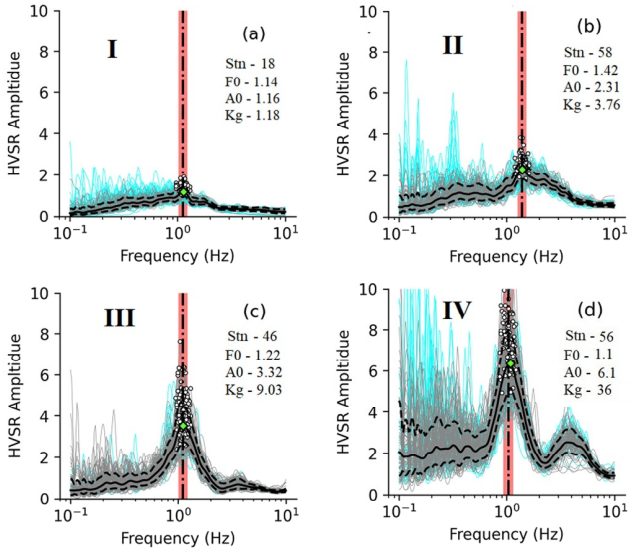

Fig.15. The HVSR observations associated with various seismically vulnerable sites according to Akkaya's (2020) classification in Equation 9. (a), (b), (c) and (d) show the sample HVSR observations for each index type.

the following relation to calculate the Seismic vulnerability index:

$$K_g = A^2 / F_0 \tag{8}$$

The K_g value indicates how vulnerable the surface layer is to displacement during earthquakes with higher K_g values indicating that the surface layer is prone to movement during earthquakes. Akkaya (2020) observed the following association of K_g values with soil deformation and earthquake damage:

$$\begin{aligned} &\text{I - } K_g \le 3 \text{ Low,} \\ &\text{II - } 3 < K_g \le 5 \text{ Moderate,} \\ &\text{III - } 5 < K_g \le 10 \text{ High,} \\ &\text{IV - } K_g \ge 10 \text{ Very high.} \end{aligned} \tag{9}$$

Sample curves for each category in Equation 9 obtained at various stations are shown in Fig.15. For all receiver locations with valid HVSR estimations, we computed the Kg values using Equation 8. Figure 16 shows the assessment of seismic vulnerability as per the

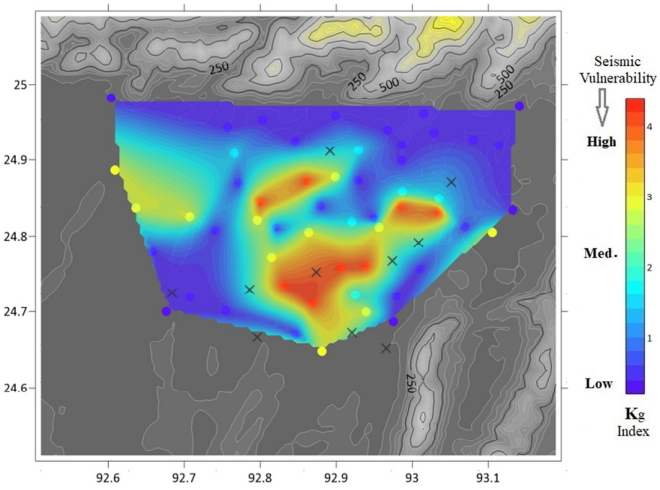

Fig.16. Seismic Vulnerability Index (Kg) distribution map of the region as per the classification given in Equation 9. Crosses indicate sites where the HVSR findings did not satisfy the reliability and stability criteria. The contours in the background are obtained from natural neighbor interpolation.

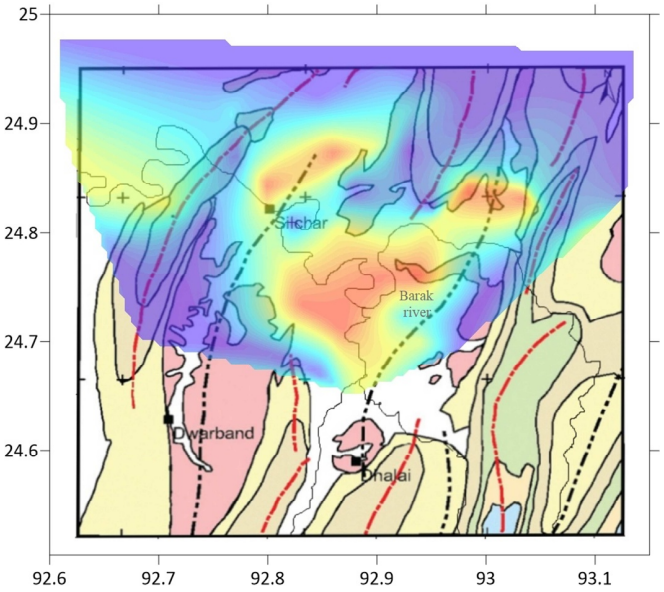

Fig.17. Seismic Vulnerability Index (Kg) distribution map of the region as per the classification given in Equation 9. Crosses indicate sites where the HVSR findings did not satisfy the reliability and stability criteria. The contours in the background are obtained from natural neighbor interpolation.

classification given in Equation 9. Figure 17 shows the results plotted in Fig.16 overlain on the geological map of the region (Figure 2). Figure 17 illustrates that the synclinal formations of the Silchar and Labak regions around the Barak river, which have a thick sediment cover of recent alluvium material, are more prone to liquefaction and seismic hazard.

Soil classes C and D are commonly associated with high Kg (Akkaya, 2020), and we also report high Kg values in regions identified with the soil classes C and D (Figs.14 & 16). The Kg value distribution also exhibits a geospatial correlation with the course of the Barak river (Figs. 2, 3 & 16). The Barak river floods often and transports a large amount of silt and has changed course in the past (Das et al. 2007). Sediment thickness and S-wave velocity have an impact on resonance frequency. The thickness of the sediment layer decreases as the resonance frequency increases, and vice versa. The amplification factor of a location is determined by the strength of the sediment layer. Weathered and weak layers demonstrate significant amplification and are at high risk of seismic hazards (Nakamura, 2000). It is recommended that tall structures should be avoided in areas with high amplification and that any significant structure built in such an area adhere to all safety measures and guidelines.

CONCLUSIONS

In the present study the seismic vulnerability of the Cachar fold-belt is characterized, a populated and important hydrocarbon-producing region located in northeast India. The HVSR analysis is performed to measure the site-effects at all the stations, which provided an estimate of the resonant frequency and the amplification factor for all the receiver locations. By analysing the results, it is observed that stations near anticlinal geo-structures have a relatively high resonance frequency and low amplification factor, whereas receivers located in synclinal areas with thick layers of alluvium sedimentary deposits show a significantly higher site amplification factor with relatively lower resonant frequencies.

An ambient noise interferometry is employed to get S-wave velocity profiles and to estimate the S-wave velocity of base-rocks, which were then used to derive estimates of S-wave velocity and thickness of top sediments based on HVSR findings. Then, we performed a regression analysis to obtain empirical relationships between resonant frequency and sediment thickness in the study region.

The seismic vulnerability index (K_g) at all the receiver locations using the results from HVSR measurements is estimated. The K_g values indicate the risk of soil liquefaction and ground and structure strains at the site. High K_g values are observed in the synclinal formations of the Silchar and Labak regions in proximity to the Barak river having a thick sediment cover of alluvium sediment of recent origin, indicating that these areas are more vulnerable to liquefaction and seismic hazard than the surrounding anticlinal regions.

Acknowledgements: The "PAN IIT-ONGC" research project helped with funding and obtaining data for the study. We would like to express our gratitude to IIT Bombay and ONGC for allowing us to publish the work.

References

Acerra, C., Havenith, H.B. and Zacharopoulos, S. (2004) Guidelines for the implementation of the H/V spectral ratio technique on ambient vibrations measurements, processing and interpretation (No. European Commission–EVG1-CT-2000-00026 SESAME). European Commission.

Akkaya, Ý. (2020) Availability of seismic vulnerability index (K g) in the assessment of building damage in Van, Eastern Turkey. Earthquake Engg. and Engineering Vibration, v.19(1), pp.189-204.

Bard, P. Y. (1999) Microtremor measurements: a tool for site effect estimation. The effects of surface geology on seismic motion. Jour. title, v.3, pp.1251-1279.

Behm, M., Leahy, G. M. and Snieder, R. (2014) Retrieval of local surface wave velocities from traffic noise–an example from the La Barge basin (Wyoming). Geophys. Prospect., v.62(2), pp.223-243.

Bensen, G. D., Ritzwoller, M. H., Barmin, M. P., Levshin, A. L., Lin, F., Moschetti, M. P., ... & Yang, Y. (2007). Processing seismic ambient noise data to obtain reliable broad-band surface wave dispersion measurements. Geophys. Jour. Internat., v.169(3), pp.1239-1260.

Bonnefoy-Claudet, S., Baize, S., Bonilla, L. F., Berge-Thierry, C., Pasten, C., Campos, J., ... & Verdugo, R. (2009) Site effect evaluation in the basin of Santiago de Chile using ambient noise measurements. Geophys. Jour. Internat., v.176(3), pp.925-937.

Census of India (2011) http://www.censusindia.gov.in/, accessed 30th June,2019.

Chatterjee, S.M., Deb, A., Rao, C.V., Reddy, P.K., Sanyal, A. and Yadagiri, K. (2006) Triangle zone geometry in Cachar thrust-fold belt, India. *In:* SEG Technical Program Expanded Abstracts 2006 (pp. 1118-1122). Society of Exploration Geophysicists.

Chávez-García, F.J. and Luzón, F. (2005) On the correlation of seismic microtremors. Jour. Geophys. Res.: Solid Earth, v.110(11). doi:10.1029/2005JB003671

Cox, B. R., Cheng, T., Vantassel, J. P. and Manuel, L. (2020). A statistical representation and frequency-domain window-rejection algorithm for single-station HVSR measurements. Geophys. Jour. Internat., v.221(3), pp.2170-2183.

Das, J.D., Dutta, T. anf Saraf, A.K. (2007) Remote sensing and GIS application in change detection of the Barak river channel, NE India. Jour. Indian Soc. Remote Sensing, v.35(4), pp.301-312.

De Ridder, S., and Biondi, B.L. (2015) Ambient seismic noise tomography at Ekofisk: Geophys., v.80, pp.B167–B176.

Delgado, J., Casado, C.L., Estevez, A., Giner, J., Cuenca, A. and Molina, S. (2000) Mapping soft soils in the Segura river valley (SE Spain): a case study of microtremors as an exploration tool. Jour. Appl. Geophys., v.45(1), pp.19-32.

Dinesh, B.V., Nair, G.J., Prasad, A.G.V., Nakkeeran, P.V. and Radhakrishna, M.C. (2010). Estimation of sedimentary layer shear wave velocity using micro-tremor H/V ratio measurements for Bangalore city. Soil Dynamics and Earthquake Engineering, v.30(11), pp.1377-1382.

Draganov, D., Campman, X., Thorbecke, J., Verdel, A. and Wapenaar, K. (2009) Reflection images from ambient seismic noise: Geophysics, v.74, pp.A63–A67.

Dziewonski, A., Bloch, S. and Landisman, M. (1969) A technique for analysis of transient seismic signals: Bull. Seismol. Soc. Amer., v.59, pp.427–444.

Fäh, D., Kind, F. and Giardini, D. (2001). A theoretical investigation of average H/V ratios. Geophys. Jour. Internat., v.145(2), pp.535-549.

Garain, S., Mitra, D., & Das, P. (2019). Detection of hydrocarbon microseepage-induced anomalies by spectral enhancements of Landsat 7 ETM+ images in part of Assam–Arakan Fold Belt, India. Jour. Petrol. Explorat. Prod. Tech., v.9(4), pp.2573-2582.

Geological Survey of India, Dasgupta, S., Narula, P.L., Acharyya, S.K. and Banerjee, J. (2000) Seismotectonic atlas of India and its environs. Geological Survey of India.

Haney, M.M., and Tsai, V.C. (2015) Nonperturbational surface-wave inversion: A Dix-type relation for surface waves. Geophysics, v.80, pp.EN167–EN177.

Haney, M.M. and Tsai, V.C. (2017) Perturbational and non-perturbational inversion of Rayleigh-wave velocities. Geophysics, v.82(3), pp.F15-F28.

Hanasoge, S. M., & Branicki, M. (2013) Interpreting cross-correlations of one-bit filtered seismic noise. Geophys. Jour. Internat., v.195(3), pp.1811-1830.

Ibs-von Seht, M. and Wohlenberg, J. (1999) Microtremor measurements used to map thickness of soft sediments. Bull. Seismol. Soc. Amer., v.89, pp.250–259.

Kayal, J. R. (2008). Microearthquake seismology and seismotectonics of South Asia. Springer Science & Business Media.

Kayal, J.R., Arefiev, S.S., Baruah, S., Hazarika, D., Gogoi, N., Gautam, J L., ... & Tatevossian, R. (2012) Large and great earthquakes in the Shillong plateau–Assam valley area of Northeast India Region: Pop-up and transverse tectonics. Tectonophysics, v.532, pp.186-192.

Krischer, L., Megies, T., Barsch, R., Beyreuther, M., Lecocq, T., Caudron, C., and Wassermann, J. (2015). ObsPy: a bridge for seismology into the scientific Python ecosystem. Computational Science & Discovery, v.8(1), 014003.

Lachetl, C. and Bard, P.Y. (1994) Numerical and theoretical investigations on the possibilities and limitations of Nakamura's technique. Jour. Phys. Earth, v.42(5), pp.377-397.

Lermo, J., and Chávez-García, F.J. (1993) Site effect evaluation using spectral ratios with only one station. Bull. Seismol. Soc. Amer., v.83(5), pp.1574-1594.

Lobkis, O. I., and Weaver, R.L. (2001) On the emergence of the Green's function in the correlations of a diffuse field. Jour. Acoust. Soc. Amer., v.110, pp.3011–3017.

McNamara, D.E. and Buland, R.P. (2004) Ambient Noise Levels in the Continental United States. Bull. Seismol. Soc. Amer., v.94(4), pp.517–1527.

Martin, E. (2020) A Linear Algorithm for Ambient Seismic Noise Double Beamforming Without Cross-correlations.

Mazumder, S., Adhikari, K., Mitra, D.S., Mahapatra, S. and Pangtey, K.K.S. (2016) A neotectonic based geomorphic analysis using remote sensing data to delineate potential areas of hydrocarbon exploration: Cachar area, Assam. Jour. Geol. Soc. India, v.88(1), pp.87-97.

Molnar, S., Cassidy, J. F., Castellaro, S., Cornou, C., Crow, H., Hunter, J. A., ... & Yong, A. (2018) Application of microtremor horizontal-to-vertical spectral ratio (MHVSR) analysis for site characterization: State of the art. Surveys in Geophysics. Geophysics, v.39(4), pp.613-631.

Mordret, A., M. Land'es, N. M. Shapiro, S. C. Singh, P. Roux,and O. I. Barkved, 2013, Near-surface study at the Valhall oil field from ambient noise surface wave tomography:Geophys. Jour. Internat., v.193, pp.1627–1643.

Mukhopadhyay, S. and Bormann, P. (2004). Low cost seismic microzonation using microtremor data: an example from Delhi, India. Jour. Asian Earth Sci., v.24(3), pp.271-280.

Mundepi, A.K. and Lindholm, C. (2009) Soft soil mapping using Horizontal to Vertical Spectral Ratio (HVSR) for seismic hazard assessment of Chandigarh city in himalayan foothills, North India. Jour. Geol. Soc. India, v.74(5), pp.551.

Nagamani, D., Sivaram, K., Rao, N.P., & Satyanarayana, H.V.S. (2020) Ambient noise and earthquake HVSR modelling for site characterization in southern mainland, Gujarat. Jour. Earth System Sci., v.129(1), pp.1-14.

Nakamura, Y. (1989) A method for dynamic characteristics estimation of subsurface using microtremor on the ground surface. Railway Technical Research Institute, Quarterly Reports, v.30(1).

Nakamura, Y. (1997, November) Seismic vulnerability indices for ground and structures using microtremor. In World Congress on Railway Research in Florence, Italy.

Nakamura, Y. (2000) Clear identification of fundamental idea of Nakamura's technique and its applications: 12th World Conference on Earthquake and Engineering. New Zealand.

Nakamura, Y. (2019) What is the Nakamura method?. Seismol. Res. Lett., v.90(4), pp.1437-1443.

Nakata, N., Chang, J.P., Lawrence, J.F. and Boue, P. (2015) Body wave extraction and tomography at Long Beach, California, with ambient-noise interferometry: Jour. Geophys. Res.: Solid Earth, v.120, pp.1159–1173.

Nath, S.K., Thingbaijam, K.K.S. and Raj, A. (2008) Earthquake hazard in Northeast India—A seismic microzonation approach with typical case studies from Sikkim Himalaya and Guwahati city. Jour. Earth System Sci., v.117(2), pp.809-831.

NEHRP (1997), Recommended Provisions For Seismic Regulations For New Buildings and Other Structures, FEMA-303, Prepared by the Building Seismic Safety Council for the Federal Emergency Management Agency, Washington, DC.

Nogoshi, M. and Igarashi, T. (1971) On the Amplitude Characteristics of Microtremor, Part II. Jour. Seismol. Soc. Japan, v.24, pp.26-40.

Obermann, A., Lupi, M., Mordret, A., Jakobsdottir, S.S. and Miller, S.A. (2016) 3D-ambient noise Rayleigh wave tomography of Snaefellsjokull volcano, Iceland: Jour. Volcanol. Geotherm. Res., v.317.

Peterson, J. (1993) Observation and modelling of seismic background noise. U.S. Geol. Surv. Tech. rept.

Parolai, S., Bormann, P., and Milkereit, C. (2002) New relationships between Vs, thickness of sediments, and resonance frequency calculated by the H/V ratio of seismic noise for the Cologne area (Germany). Bull. Seismol. Soc. Amer., v.92(6), pp.2521-2527.

Rickett, J. and Claerbout, J.F. (1999) Acoustic daylight imaging via spectral factorization: Helioseismology and reservoir monitoring: The Leading Edge, v.18, pp.957–960.

Rigo, A., Sokos, E., Lefils, V. and Briole, P. (2021) Seasonal variations in amplitudes and resonance frequencies of the HVSR amplification peaks linked to groundwater. Geophys. Jour. Internat., v.226(1), pp.1-13.

Saha, D., Bahguna, C.S., Prabhakarudu, J.N. and Baloni, C.L. (2008) Significance of gravity and magnetic data over thrust-fold area–A case study in the Cachar area of Surma sub-basin of Assam–Arakan Basin, Assam, India. *In* 7th Int. Conf. & Exposition on Petroleum Geophysics, Hyderabad, India (pp.145-151).

SESAME. (2004) Guidelines for the Implementation of the H/V Spectral Ratio Technique on Ambient Vibrations Measurements, Processing, and Interpretation. (No. WP12-Deliverable D23.12; p.62). European Commission - Research General Directorate.

Shapiro, N.M. and Campillo, M. (2004) Emergence of broad-band Rayleigh waves from correlations of the ambient seismic noise.: Geophys. Res. Lett., v.31, L07614.

Shapiro, N. M., Campillo, M., Stehly, L., & Ritzwoller, M. H. (2005). High-resolution surface-wave tomography from ambient seismic noise. Science, v.307(5715), pp.1615–1618.

Sivaram, K., Mahesh, P., & Rai, S.S. (2012). Stability assessment and quantitative evaluation of H/V spectral ratios for site response studies in Kumaon Himalaya, India using ambient noise recorded by a broadband seismograph network. Pure and Appl. Geophys., v.169(10), pp.1801-1820.

Snieder, R., 2004, Extracting the Green's function from the correlation of coda waves: A derivation based on stationary phase: Phys. Rev. E, v.69, 046610.

Surve, G., & Mohan, G. (2010) Site response studies in Mumbai using (H/V) Nakamura technique. Natural Hazards, v.54(3), pp.783-795.

Sylvette, B. C., Cécile, C., Pierre-Yves, B., Fabrice, C., Peter, M., Jozef, K., & Fäh, D. (2006). H/V ratio: a tool for site effects evaluation. Results from 1-D noise simulations. Geophys. Jour. Internat., v.167(2), pp.827-837.

Vantassel, J. (2020) http://doi.org/10.5281/zenodo.3666956, Zenodo. jpvantassel/hvsrpy: latest (Concept).

Walling, M. Y., & Mohanty, W. K. (2009) An overview on the seismic zonation and microzonation studies in India. Earth-Sci. Rev., v.96(1-2), pp.67-91.

Wapenaar, K. (2004) Retrieving the Elastodynamic Green's Function of an Arbitrary Inhomogeneous Medium by Cross Correlation: Phys. Rev. Lett., v.93.

Yang, Y., & Ritzwoller, M. H. (2008) Characteristics of ambient seismic noise as a source for surface wave tomography. Geochem., Geophys., Geosyst., v.9(2).

Yao, H., X. Campman, M. V. de Hoop, and R. van der Hilst (2009) Estimation of surface wave Green's functions from correlation of direct waves, coda waves, and ambient noise in SE Tibet: Phys. Earth Planet. Inter., v.77, pp.1–11.

Zigone, D., Y. Ben-Zion, M. Campillo, and P. Roux, 2015, Seismic Tomography of the Southern California Plate Boundary Region from Noise-Based Rayleigh and Love Waves: Pure and Applied Geophysics, 172, 1007–1032.